



ELSEVIER

Available online at www.sciencedirect.com

SCIENCE @ DIRECT®

Nuclear Instruments and Methods in Physics Research A 496 (2003) 102–122

**NUCLEAR
INSTRUMENTS
& METHODS
IN PHYSICS
RESEARCH**
Section Awww.elsevier.com/locate/nima

Analog Cherenkov detectors used in laser spectroscopy experiments on antiprotonic helium

M. Hori^{a,*}, K. Yamashita^{b,1}, R.S. Hayano^b, T. Yamazaki^c^a CERN, EP Division, CH-1211 Geneva 23, Switzerland^b Department of Physics, University of Tokyo, 7-3-1 Hongo, Bunkyo-ku, Tokyo 113-0033, Japan^c The Institute of Physical and Chemical Research (RIKEN), Wako, Saitama 351-0198, Japan

Received 19 July 2002; received in revised form 21 August 2002; accepted 27 August 2002

Abstract

We describe some acrylic Cherenkov detectors read out by gateable fine-mesh photomultipliers, used in laser spectroscopy experiments of metastable antiprotonic helium ($\bar{p}\text{He}^+$) atoms carried out at the LEAR and AD facilities at CERN. The atoms were produced by stopping pulsed antiproton beams in a helium target. Charged particles emerging from the antiproton annihilations produced Cherenkov light in the detector, the time envelope of which consisted of a strong flash from the promptly-annihilating antiprotons, followed by a much longer but less intense tail from the delayed annihilations of the metastable atoms. The photomultiplier was turned off during the initial light flash by reversing the electric potential on its dynodes, thus allowing only the delayed annihilations to be recorded as an analog pulse. The atoms were irradiated with a laser pulse tuned to the characteristic wavelength which stimulated antiproton transitions from a metastable state to a state with a short lifetime against annihilation. The resonance condition between the laser beam and the atom was thus revealed as a sharp spike superimposed on the Cherenkov light pulse. We tested Cherenkov radiators of various sizes and different types of photomultipliers in order to (i) suppress the spurious afterpulsing in the photomultiplier signal caused by the strong flash of Cherenkov light during the prompt annihilation, (ii) evaluate the background caused by $\pi^+ \rightarrow \mu^+ \rightarrow e^+$ decay, and (iii) optimize the linearity, dynamic range, and response time of the detector.

© 2003 Elsevier Science B.V. All rights reserved.

PACS: 36.10. - k; 42.62.Fi; 29.40.Ka; 85.60.Ha

Keywords: Cherenkov detector; Antiprotonic helium atom; Fine mesh photomultiplier; Afterpulse

1. Introduction

When antiprotons are stopped in a helium target, some 3% of them survive with an anomalously long lifetime of $\tau = 3 - 4 \mu\text{s}$ [1,2]. This is due to the formation of metastable antiprotonic helium ($\bar{p}\text{He}^+$) atoms, which are three-body Coulomb systems composed of a helium nucleus, an antiproton, and an electron. In this paper, we describe analog Cherenkov detectors which were developed to observe antiproton annihilations in laser spectroscopy experiments on this atom. The measurements were made using high-intensity

*Corresponding author. Tel.: +41-22-767-8306; fax: +41-22-767-3500.

E-mail address: masaki.hori@cern.ch (M. Hori).

¹ Present address: Matsushita Electric Industrial Co. Ltd., 1006 Oaza Kadoma, Kadoma-shi, Osaka 571-8501, Japan.

pulsed beams of antiprotons produced at the Low Energy Antiproton Ring (LEAR) and Antiproton Decelerator (AD) facilities of CERN.

The energy level diagram of the $\bar{p}\text{He}^+$ atom is shown in Fig. 1(a), with metastable states (those having microsecond-scale lifetimes) indicated in solid lines. These states have such large principal ($n \sim 38$) and angular momentum ($\ell \sim n$) quantum numbers, that antiprotons captured into them cannot easily deexcite by Auger emission of the remaining electron. They instead deexcite by radiating a series of optical-frequency photons (the theoretical wavelengths [3] of which are shown in Fig. 1(a) in nanometers), as the antiproton traverses through a constant- $v = n - \ell - 1$ cascade of metastable states (indicated by arrows). Finally the atom reaches a short-lived state (shown in wavy lines), which leads to Auger emission of the second electron within nanoseconds. The antiproton proceeds to a $\bar{p}\text{He}^{2+}$ ionic state, and

annihilates within picoseconds. The Cherenkov detectors described here were developed to observe these annihilations.

In previous papers [4–6], we have described an experiment to measure the delayed annihilation time spectrum (the distribution of the number of antiproton annihilations, as a function of the time elapsed since atom formation, see Fig. 1(b)). A continuous beam of some 10^4 \bar{p} /s was stopped in a helium target, thus producing $\bar{p}\text{He}^+$ atoms in an event-by-event manner. Each atom was irradiated with a laser pulse tuned to the characteristic wavelength which stimulated an antiproton transition between pairs of metastable and Auger-dominated states [4,5]. This forced the immediate annihilation of otherwise long-lived antiprotons, thereby revealing the resonance condition between the laser beam and the atom as a sharp spike superimposed on the delayed annihilation time spectrum. In Fig. 1(c), an annihilation

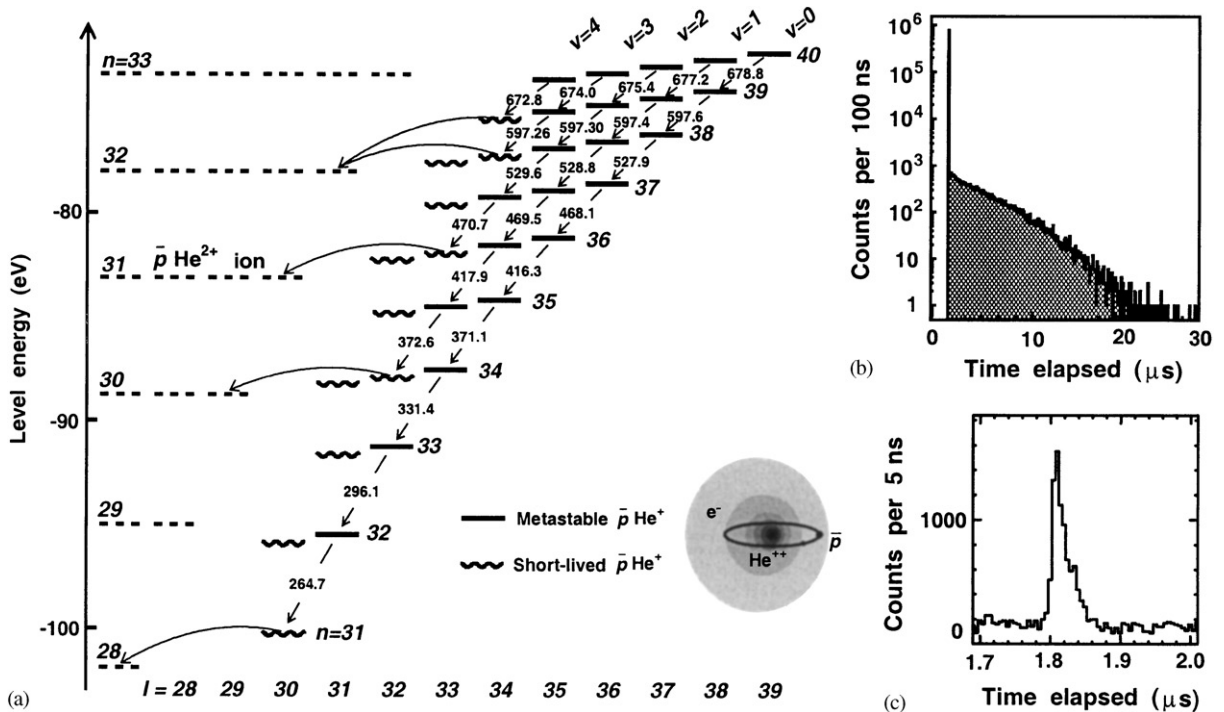


Fig. 1. Energy level structure of $\bar{p}\text{He}^+$ atoms (a). Solid lines indicate metastable levels, wavy lines Auger-dominated short-lived ones. Broken lines show $\bar{p}\text{He}^{2+}$ ionic states formed after Auger electron emission. On the left-hand side theoretical absolute energies of each state are shown relative to the three-body breakup threshold [3]. The wavelengths of radiative transitions following the propensity rule $v = n - \ell - 1 = \text{const}$ (see text) is expressed in nanometers. Delayed annihilation time spectrum of $\bar{p}\text{He}^+$ (b). Laser-induced annihilation spike of the transition $(n, \ell) = (39, 35) \rightarrow (38, 34)$ at a wavelength of $\lambda = 597.26$ nm (c).

spike corresponding to the transition $(n, \ell) = (39, 35) \rightarrow (38, 34)$ at a wavelength of $\lambda = 597.26$ nm is shown, induced by firing the laser at a time $t = 1.8$ μ s after atomic formation. This technique was successful and led to accurate measurements on the atomic transition energies [5,7], state lifetimes [8], and populations [9] of $\bar{p}\text{He}^+$.

In 1994, a short experiment [10] was made at LEAR to test the feasibility of making laser spectroscopy of $\bar{p}\text{He}^+$ using pulsed [11,12], rather than continuous, antiproton beams. A 250-ns-long pulse containing some 1×10^8 antiprotons was stopped in the helium target, thus producing $\sim 3 \times 10^6$ metastable $\bar{p}\text{He}^+$ atoms simultaneously. Charged particles emerging from the annihilations produced Cherenkov light in an acrylic plate placed near the target. The envelope of the resulting light pulse consisted of an extremely bright, 250-ns-long flash from the promptly annihilating antiprotons, followed by a much longer but less intense tail from delayed annihilations of the metastable atoms. This tail corresponds to the spectrum shown in Fig. 1(b) and (c) in the continuous beam case. By irradiating the atoms with a single laser pulse, a spike corresponding to the superposition of many simultaneous annihilations was induced on the tail. The light pulse was detected by a line-focus photomultiplier in which the electron multiplication was gated off during the initial 250-ns-long flash. One advantage of this method was that large numbers of $\bar{p}\text{He}^+$ atoms could be produced and studied at a higher rate than was possible using continuous antiproton beams. Another was that the laser could be timed to fire immediately after the arrival of the antiproton pulse, thus allowing the atomic states to be studied at times immediately after their formation; by contrast, in experiments using continuous antiproton beams, the laser could be fired only after a minimum delay $t = 1.8$ μ s (Fig. 1(c)) due to the technical reasons described in Section 7.

The test experiment, however, revealed serious problems in the Cherenkov detector that made qualitative studies of $\bar{p}\text{He}^+$ atoms difficult: (i) the measured spectra were highly distorted and contained spurious afterpulses caused by the strong flash of Cherenkov light irradiating the photo-

cathode during the prompt annihilation, (ii) the spectra contained a large background due to the positive pions stopping in the material surrounding the target and undergoing $\pi^+ \rightarrow \mu^+ \rightarrow e^+$ decay, (iii) the reproducibility of the experiment was poor, primarily due to the non-linear response of the photomultiplier.

This work reports on the development of a series of Cherenkov detectors which overcame these problems and allowed the measurement of very weak, previously undetected $\bar{p}\text{He}^+$ transitions in experiments carried out at LEAR [13,14]. The detectors were also used in recent experiments made at AD [15,16], in which the atomic transition frequencies of $\bar{p}\text{He}^+$ were measured to a fractional precision of 1.3×10^{-7} [17]. By analyzing the observed profiles of the laser-induced annihilation spikes, the quenching of $\bar{p}\text{He}^+$ states due to collisions with deuterium molecules [18], and their Auger lifetimes [19] were also studied. The primary populations of the atom were derived [20] by firing the laser at various times t , and measuring the intensities of the resulting annihilation spikes at each of them.

This paper is organized as follows: in Section 2, the construction of the Cherenkov detector used in the LEAR experiments are described. Two test experiments (Section 3) were carried out at the 1.3-GeV electron synchrotron of the High Energy Accelerator Research Organization (KEK) Tanashi Campus, to calibrate the detector's yield of photoelectrons per incident particle, and the linearity versus high-intensity pulsed beams. Monte Carlo simulations (Section 4) were made to estimate the intensity of the Cherenkov light produced by the delayed annihilations, and the background due to $\pi^+ \rightarrow \mu^+ \rightarrow e^+$ decay. The gateable fine-mesh photomultiplier used to detect the Cherenkov light is described in Section 5. The afterpulsing of various photomultipliers were studied by injecting strong flashes of light into them. In Section 6, delayed annihilation time spectra measured using the detector are shown. The results are compared with those of previous experiments using continuous antiproton beams in Section 7. In Section 8, we describe Cherenkov detectors used in recent experiments carried out at AD, together with some typical results.

2. Cherenkov detector design

The layout of the laser spectroscopy experiment of $\bar{p}\text{He}^+$ carried out at LEAR is shown in Fig. 2(a). Pulsed beams containing between 5×10^7 and 1×10^9 antiprotons with a pulse-length of $\Delta t = 250$ ns were stopped in a cryogenic helium target, thus producing between 2×10^6 and 3×10^7 metastable $\bar{p}\text{He}^+$ atoms. The spatial XY profile, intensity, and time structure of each antiproton pulse was measured using a parallel plate ionization chamber (PPIC) [21], which was placed in the beam just upstream of the target. The target chamber [8] was a stainless steel cylinder 70 mm in diameter and 150 mm in length, into which the antiprotons entered through a 0.5-mm thick copper-beryllium window. The laser beam entered the target through a fused silica window affixed to the opposite end of the chamber. The target was filled with helium gas of 99.999% purity, at pressures between $P = 0.1$ and 10 bars, and temperatures between $T = 5$ and 30 K.

The Cherenkov detector (Fig. 2(b)) consisted of two acrylic (Bicron BC-800 methyl methacrylate monomer) plates measuring $900 \text{ mm} \times 300 \text{ mm} \times 20 \text{ mm}$ covering a total solid angle of 1.2π steradians seen from the target. They had a refractive index of $n = 1.49$, so that charged particles having velocities greater than $\beta \sim 0.7$ (corresponding to a π -meson of momentum $p \geq 130 \text{ MeV}/c$) produced Cherenkov light in them. The optical transmission of a 20-mm-thick plate was $T \sim 90\%$ at all visible and ultraviolet wavelengths longer than $\lambda = 350 \text{ nm}$, but the transmission decreased to $T \sim 70\%$ at $\lambda = 300 \text{ nm}$. The surfaces of the plates were diamond-polished and wrapped by a 4- μm -thick inner layer of aluminum foil and a 100- μm -thick outer layer of blackened plastic [22]. Light guides made of the same material coupled the Cherenkov light into the 34-mm-diam photocathode of the photomultiplier. The analog waveform of the anode signal was recorded using a digital oscilloscope (Hewlett-Packard HP54542A) with an analog bandwidth of

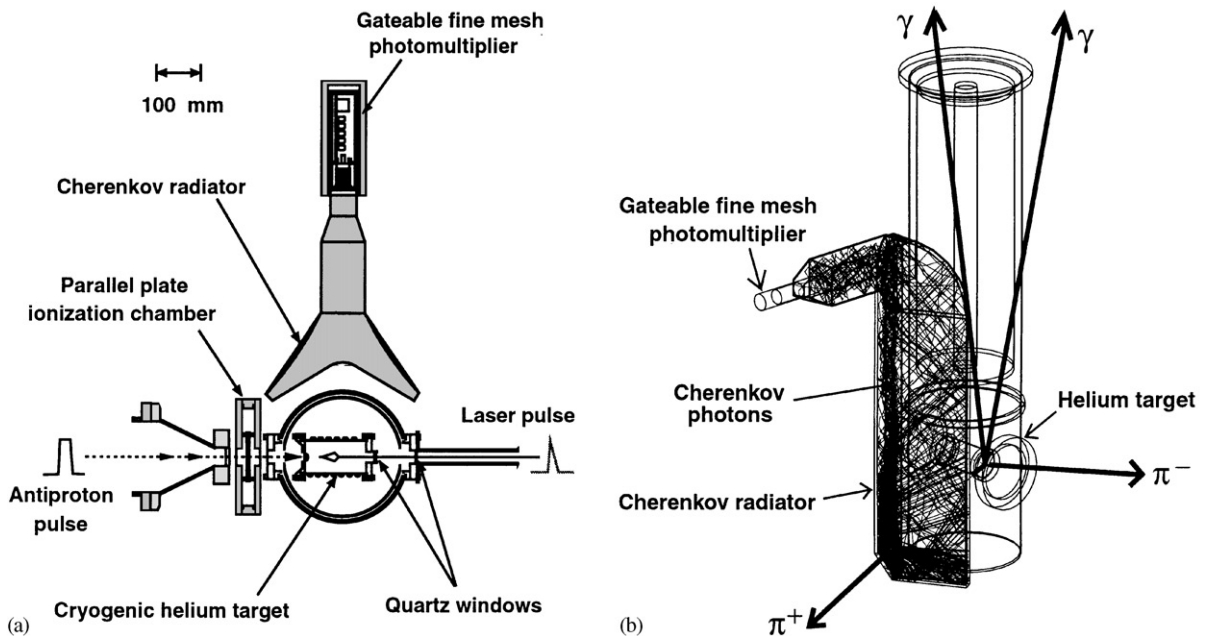


Fig. 2. Layout of the laser spectroscopy experiment of $\bar{p}\text{He}^+$ using pulsed antiproton beams (a). Monte Carlo simulation of an antiproton annihilation (b). A pair of π^+ and π^- particles, two γ -rays, and Cherenkov photons propagating inside the acrylic radiator are seen.

$f = 500$ MHz, a digital sampling rate of $f = 2$ GHz, and a digitizing resolution of 8 bits.

3. Detector tests at the 1.3-GeV electron synchrotron

The layout of the calibration experiment made to determine the number of photoelectrons emitted by the photocathode, per charged particle impinging on the Cherenkov detector is shown in Fig. 3 (bottom right). The measurements were carried out using the $\gamma - 3$ beamline at the 1.3-GeV electron synchrotron (Fig. 3, left) at KEK-Tanashi. A beam of Bremsstrahlung γ -rays was extracted from the synchrotron by moving an internal radiator target into the orbiting electrons. The beam impinged on a second target positioned a few meters downstream in the beamline, thus producing a secondary beam of electrons and

positrons. A bending magnet and lead collimator were then used to define a 10-mm-diam electron beam of kinetic energy $T = 0.6$ GeV and intensity $1000 e^-/s$. The Cherenkov detector was mounted on a motorized XYZ stage and placed in this beam. Two 5-mm-thick scintillation counters (which provided the “start” and “stop” signals), and two 10-mm-thick counters with 10-mm-diam holes in their centers (providing the “veto” signals) were placed upstream and downstream of the Cherenkov detector. To define a well-collimated beam and reject background, only those electrons that traversed the “start” and “stop” counters without hitting the “veto” counters were accepted by the data acquisition system. Furthermore, the time interval between the “start” and “stop” signals (measured by a LeCroy 2228A time-to-digital converter) were required to correspond to the time-of-flight of a 0.6-GeV electron. The Cherenkov light was detected by a 2-in. line-focus

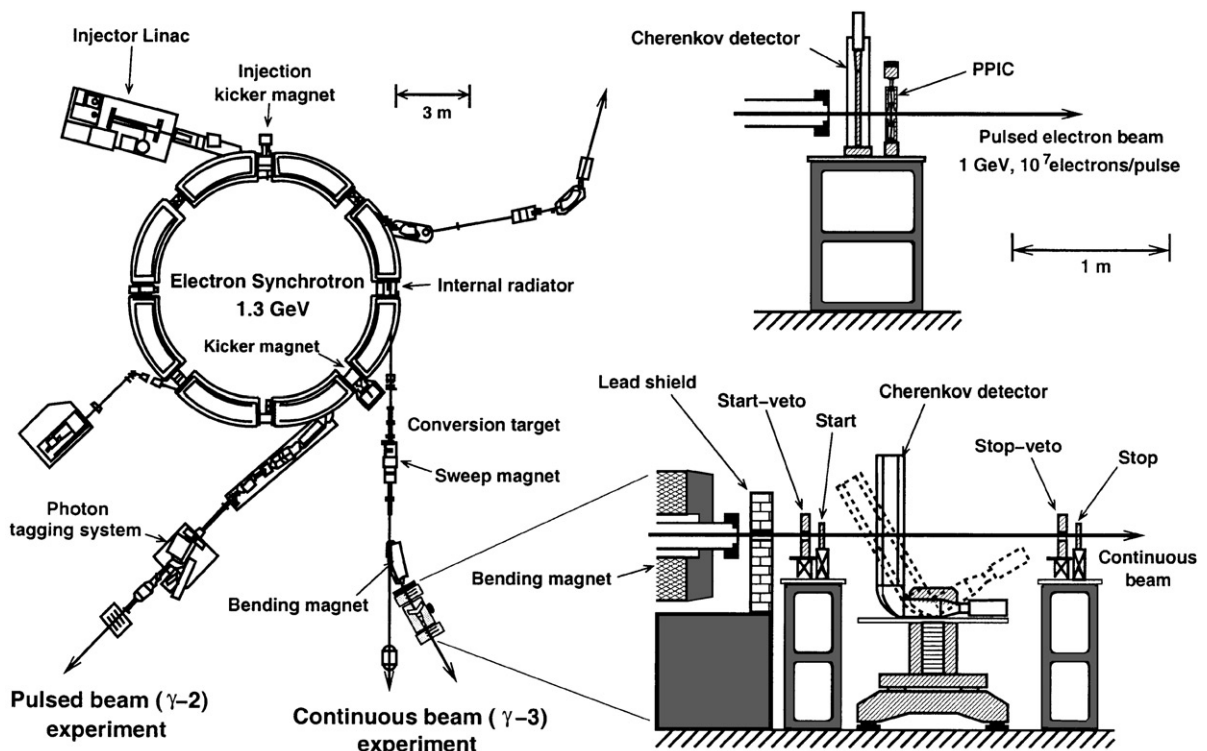


Fig. 3. Layout of two test experiments carried out at the 1.3-GeV electron synchrotron of KEK-Tanashi. One of these was made at the $\Gamma - 2$ beamline (top right) using a pulsed electron beam to measure the linearity of the Cherenkov detector. The other experiment was carried out at the $\Gamma - 3$ beamline using a continuous electron beam to calibrate the light-yield of the detector.

photomultiplier (Hamamatsu Photonics R329-PSX) which was specially selected by the manufacturer for high photon resolution. Measurements with a single-photon light source made prior to the experiment showed that the photomultiplier could distinguish the signals corresponding to one or two photoelectrons emitted simultaneously from the photocathode. The anode output was amplified by a low-noise voltage amplifier (Phillips Scientific 6954-B-20) with a gain of $g = 20$ and a bandwidth of $f = 1.5$ GHz. The intensity of each photomultiplier pulse was measured using a charge-sensitive analog-to-digital converter (LeCroy 2249A).

The three pulse-height distributions shown in Fig. 4 were obtained by positioning the detector at different angles θ relative to the electron beam as

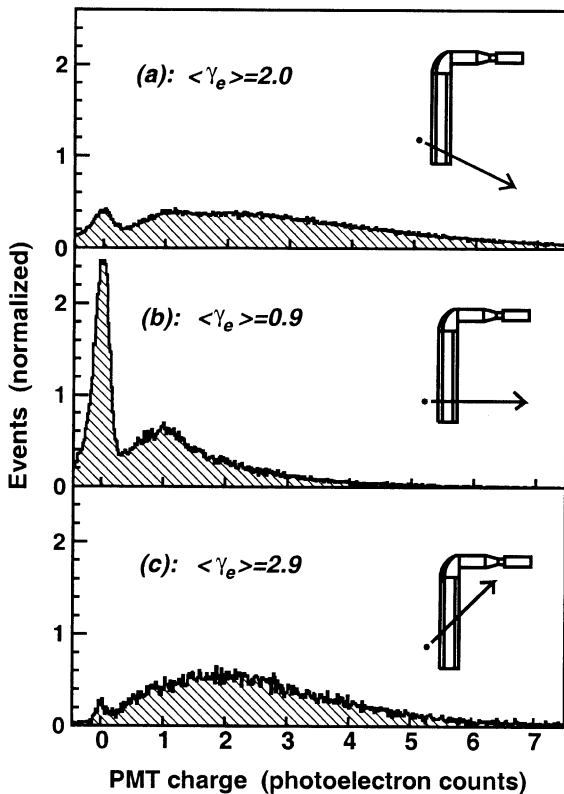


Fig. 4. Pulse-height distributions of the Cherenkov detector, corresponding to three different incident angles of the 0.6-GeV electron beam (a)–(c). The filled circle represent the position of the helium target in the $\bar{p}\text{He}^+$ experiment. The mean number of photoelectrons $\langle \gamma_e \rangle$ produced per incident 0.6-GeV electron is shown on each histogram.

indicated in the right corner of each histogram. The filled circle in each figure represents the position of the helium target. By using the fact that the pulse-heights follow a Poisson statistical distribution, the mean numbers of photoelectrons $\langle \gamma_e \rangle$ produced per 0.6-GeV electron was estimated. This varied from $\langle \gamma_e \rangle = 0.9$ when the beam was perpendicular ($\theta = 90^\circ$) to the detector surface, to $\langle \gamma_e \rangle = 2.9$ at an incident angle of $\theta = 45^\circ$. By moving the Cherenkov detector using the XYZ stage, the position-dependence of $\langle \gamma_e \rangle$ was systematically measured over its entire surface.

A separate experiment was made at the γ -2 beamline (Fig. 3, upper right) to study the response of the Cherenkov detector to high-intensity electron beams. Using a kicker magnet, we extracted 2–4- μs -long pulses of electrons with peak intensities between $I = 3$ pA and 40 nA, and energy $T = 1$ GeV from the synchrotron. The beam was directed at the detector, and the resulting Cherenkov light was measured by a fine-mesh photomultiplier (Hamamatsu Photonics R5504GX-ASSY). All oscilloscope traces of photomultiplier signals in this paper are plotted with their polarities inverted. As shown in the anode waveforms of Fig. 5(a) and (b), the 1-GeV electrons could be resolved as individual pulses and counted at beam intensities below $I = 100$ pA. As the beam intensity was increased above $I = 100$ pA (Fig. 5(c) and (d)), however, individual events could no longer be resolved and the anode signal took on a continuous shape corresponding to the envelope of the pulsed electron beam. A parallel plate ionization chamber was used to measure the absolute beam intensities above $I = 1$ nA. In Fig. 3(e), the number of photoelectrons produced per 1-GeV electron pulse is plotted; a linear response spanning five orders of magnitude, between 2×10^3 and 3×10^7 photoelectrons per pulse was observed. The upper limit corresponds to the maximum number of photoelectrons expected in the $\bar{p}\text{He}^+$ experiments.

4. Monte Carlo simulations

Monte Carlo simulations were made to estimate the intensity and time profile of the Cherenkov

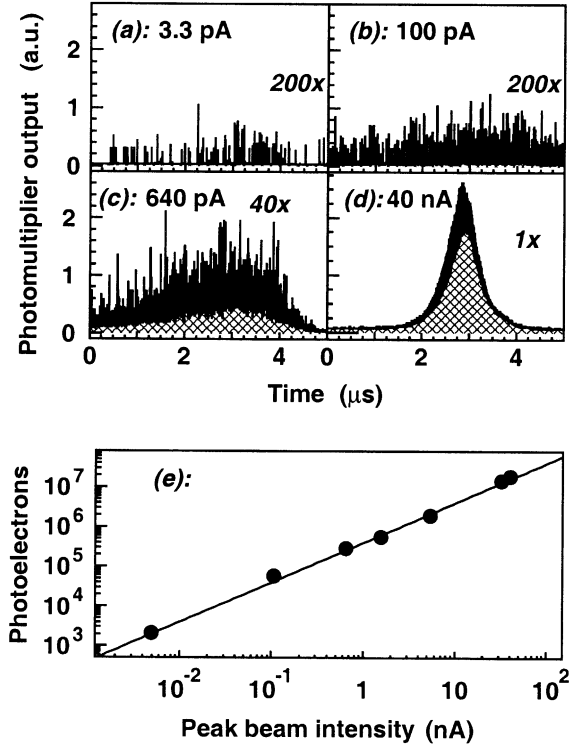


Fig. 5. The response of the Cherenkov detector for pulsed electron beams with peak intensities between $I = 3$ pA and 40 nA (a)–(d). Note factor 1, 40, and 200 differences in the Y-axis scales. Number of photoelectrons produced at various intensities of the electron beam (e).

light produced by the delayed annihilations, and the contribution of the background due to $\pi^+ \rightarrow \mu^+ \rightarrow e^+$ decay. The simulation required (i) the mean photoelectron yield $\langle \gamma_e \rangle$ measured above, (ii) detailed knowledge on the numbers and momentum distributions of the secondary particles (mostly π -mesons, electrons, and positrons) produced when antiprotons annihilate on a helium nucleus. Unfortunately, although experimental data [23,24] for certain channels of this reaction have been recently published (Table 1), no complete set of branching ratios exist. We therefore estimated the yields of secondary particles by combining three sets of experimental data: (i) the branching ratios for antiprotons annihilating on protons [25–31], (ii) the experimental data for antineutrons annihilating on protons, from which we inferred the branching ratios for antiprotons

Table 1

Secondary particles produced in $\bar{p} + p$, $\bar{p} + n$, and $\bar{p} + {}^4\text{He}$ reactions, and their experimental branching ratios shown in percentages. Protons with momenta $P > 300$ MeV/c are denoted by p_f

Branching ratios (%) for $\bar{p} + p$	
$2\pi^0$	0.0693 ± 0.0043 [25]
$n\pi^0$ ($n \geq 1$)	$4.1_{-0.6}^{+0.2}$ [26–28]
$\pi^+ + \pi^-$	0.307 ± 0.013 [25]
$\pi^+ + \pi^- + \pi^0$	5.82 ± 0.43 [29]
$\pi^+ + \pi^- + 2\pi^0$	9.3 ± 3.0 [26–28]
$\pi^+ + \pi^- + 3\pi^0$	23.3 ± 3.0 [26–28]
$\pi^+ + \pi^- + 4\pi^0$	2.8 ± 0.7 [26–28]
$2\pi^+ + 2\pi^-$	6.9 ± 0.6 [26–28]
$2\pi^+ + 2\pi^- + \pi^0$	19.6 ± 0.7 [26–28]
$2\pi^+ + 2\pi^- + 2\pi^0$	16.6 ± 1 [26–28]
$2\pi^+ + 2\pi^- + 3\pi^0$	4.2 ± 1 [26–28]
$3\pi^+ + 3\pi^-$	2.1 ± 0.25 [26–28]
$3\pi^+ + 3\pi^- + \pi^0$	1.85 ± 0.15 [26–28]
$3\pi^+ + 3\pi^- + n\pi^0$	0.3 ± 0.1 [28]
$(n \geq 2)$	
$K^+ + K^- + K^0$	0.237 ± 0.016 [30]
$K^+ + K^- + \pi^0$	0.237 ± 0.015 [31]
$K^\pm + K^0 + \pi^\mp$	0.46 ± 0.07 [30]
$K^\pm + K^0 + \pi^\mp + \pi^0$	0.47 ± 0.06 [31]
$K^+ + K^-$	0.099 ± 0.005 [25]
Branching ratios (%) for $\bar{p} + n$	
$\pi^- + n\pi^0$	16.4 ± 0.5 [32,28]
$(n \geq 1)$	
$\pi^- + \pi^0$	~ 0.8 [33]
$2\pi^- + \pi^+ + n\pi^0$	59.7 ± 1.2 [32,28]
$(n \geq 0)$	
$2\pi^- + \pi^+$	3.4 ± 0.2 [33]
$2\pi^- + \pi^+ + \pi^0$	17 ± 2 [33]
$3\pi^- + 2\pi^+ + n\pi^0$	23.4 ± 0.7 [32,28]
$(n \geq 1)$	
$3\pi^- + 2\pi^+$	4.2 ± 0.2 [33]
$3\pi^- + 2\pi^+ + \pi^0$	15.1 ± 1.0 [32]
$4\pi^- + 3\pi^+ + n\pi^0$	0.39 ± 0.07 [32,28]
$(n > 0)$	
Branching ratios (%) for $\bar{p} + {}^4\text{He}$	
$\sigma(\bar{p}n)/\sigma(\bar{p}p)$	42 ± 5 [34]
$2\pi^+ + 2\pi^-$	2.752 ± 0.372 [23]
$2\pi^+ + 2\pi^- + n\pi^0$ ($n \geq 1$)	20.9 ± 1.9 [23]
$2\pi^+ + 2\pi^- + p_f$	0.343 ± 0.065 [23]
$2\pi^+ + 2\pi^- + p_f + n\pi^0$ ($n \geq 1$)	3.08 ± 0.35 [23]
$3\pi^+ + 2\pi^-$	1.97 ± 0.32 [23]
$\pi^+ + 2\pi^- + 2p_f$	0.856 ± 0.096 [23]
$2\pi^- + 3p_f$	0.063 ± 0.010 [23]

annihilating on neutrons [32,33], (iii) the experimental observation that in the nuclear reaction $\bar{p} + {}^4\text{He}$, the ratio between the number of

antiprotons that annihilate on the neutrons of a helium nucleus, and those that annihilate on the protons is $\sigma(\bar{p}n)/\sigma(\bar{p}p) = 0.42 \pm 0.05$ [34]. We estimate that on average 1.5 π^+ -mesons, 1.8 π^- -mesons, and 2 π^0 -mesons are produced in a $\bar{p} + {}^4\text{He}$ reaction. The π^0 's decay into two γ -rays with a 0.08-fs lifetime [35] while still inside the helium target. About 30% of the γ -rays are converted into electron and positron pairs while traveling through the target walls, and some of these produce Cherenkov light in the detector.

A simplified model was used to simulate the momentum distributions of the secondary particles. Each annihilation deposited a total energy $E_{\text{tot}} = 1.9$ GeV and produced mesons according to the branching ratios given in Table 1. The momentum vectors P_i of the mesons with rest masses M_i were calculated by distributing the total kinetic energy $T_{\text{tot}} = E_{\text{tot}} - \sum_i M_i$ among the particles, assuming a relativistic phase-space distribution. Nuclear fragments [36] produced in reactions such as $\bar{p} + {}^4\text{He} \rightarrow {}^3\text{He}$ or $\bar{p} + {}^4\text{He} \rightarrow {}^2\text{H}$ were assumed to recoil with an energy of about $T = 5\text{--}10$ MeV. To test the accuracy of this simulation, the measured momentum distribution of π^- -mesons produced in a $\bar{p} + {}^4\text{He}$ reaction [37] was compared with the corresponding distribution generated by the simulation (Fig. 6). In the high-momentum region ($p = 0.15\text{--}1.0$ GeV/c), the two distributions agreed within the error bars and reached a maximum at $p \sim 0.2$ MeV/c. At lower momenta ($p < 0.1$ GeV/c), however, the experimental yields were $\sim 50\%$ lower than simulation, presumably due to final-state nuclear interactions which have been neglected here.

Using the GEANT 4.0 [38] simulation package, a three-dimensional computer model of the cryogenic target, Cherenkov detector, and surrounding material was generated (Fig. 2(b)). The trajectories of all the particles produced in the annihilation were followed for 15 μs . The important decay and reaction processes were accurately simulated, such as $\pi^\pm \rightarrow \mu^\pm \rightarrow e^\pm$ and $\pi^0 \rightarrow 2\gamma$ decays, multiple scattering, ionization, Bremsstrahlung, e^+e^- annihilation and pair creation. The propagation of Cherenkov photons inside the detector was simulated (Fig. 2(b)) taking into account the optical attenuation, reflection, and scattering inside the

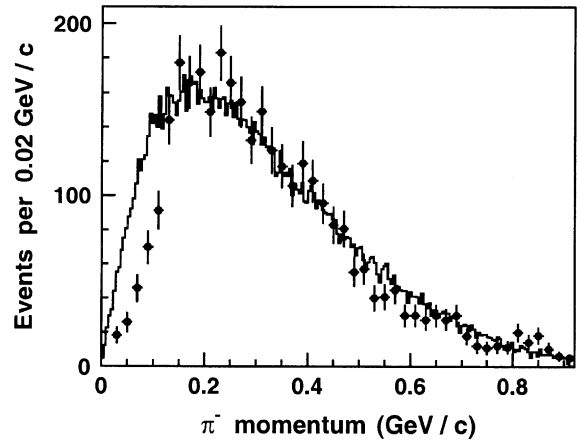


Fig. 6. Simulated momentum distribution of π^- -mesons produced by antiprotons annihilating on a ${}^4\text{He}$ nucleus (solid lines). Experimental data [36] are shown superimposed.

radiator [22]. The quantum efficiency and time response of the photomultiplier was measured, and their effects were included in the simulation. Some 6×10^6 simulated annihilations were calculated over a period of 150 h using two workstations (Digital Equipment Corporation AlphaStation 600-5/333 and AlphaPC 164). In Fig. 7(a), the simulated distribution of the number of photoelectrons $\gamma_{\bar{p}}$ produced per antiproton annihilation is shown. No photoelectrons were detected in $\sim 25\%$ of the annihilations, whereas in 1% of the cases more than $\gamma_{\bar{p}} = 10$ photoelectrons were produced by charged particles striking the light guide near the photocathode. A mean photoelectron yield of $\langle \gamma_{\bar{p}} \rangle = 1.9$ was derived.

In Fig. 7(b), the simulated time spectrum of Cherenkov photoelectrons produced by 6×10^6 antiprotons annihilating at $t = 0$ is shown. Although the vast majority of the photoelectrons were produced at $t = 0$ in coincidence with the annihilations, delayed photoelectrons were also observed, the light envelope of which decayed with a mean lifetime of $\tau = 2.2$ μs . These delayed photoelectrons constituted a major source of background; they could not be distinguished from the signal produced by the metastable $\bar{p}\text{He}^+$ atoms, which contained multiple decay components with lifetimes of $\tau = 0.2\text{--}5$ μs [1,2]. The background was produced when some of the

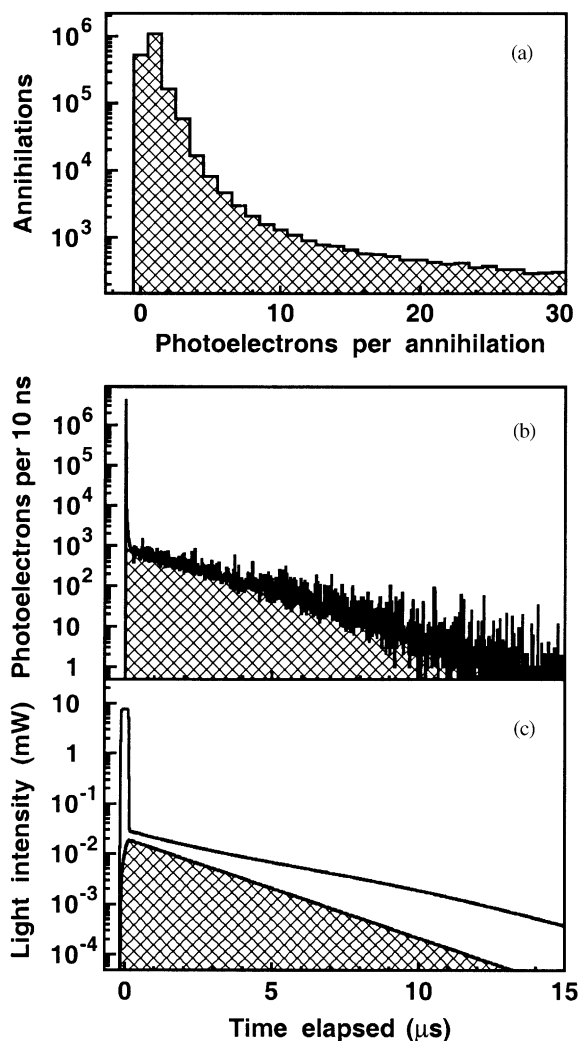


Fig. 7. Simulated distribution of the number of photoelectrons produced in the Cherenkov detector by an antiproton annihilation (a). Simulated time spectrum of photoelectrons produced by 6×10^6 antiprotons annihilating at $t = 0$ (b). The envelope of the Cherenkov light produced when a pulse containing 5×10^8 antiprotons is stopped in the helium target (c). The hatched area corresponds to the background caused by $\pi^+ \rightarrow \mu^+ \rightarrow e^+$ decay.

low-energy π^+ -mesons emerging from the annihilations stopped in the target walls or in the detector. These decayed into positive muons with a mean lifetime of $\tau = 26$ ns [35], and further decayed into positrons with a 2.2- μ s lifetime. Some of these positrons with a mean energy of

$T = 40$ MeV struck the detector and produced delayed photoelectrons.

In Fig. 7(c), the envelope of Cherenkov light that reaches the photocathode is shown, simulated for a pulse containing 5×10^8 antiprotons stopping in the helium target. This spectrum was synthesized by (i) taking the delayed annihilation time spectrum (Fig. 1(b)) measured in past experiments using continuous antiproton beams, (ii) adding the $\pi^+ \rightarrow \mu^+ \rightarrow e^+$ background, (iii) normalizing the spectrum with the mean photoelectron yield ($\langle \gamma_{\bar{p}} \rangle = 1.9$) estimated above. The resulting spectrum consisted of a 250-ns-long flash with a peak intensity of $I = 5$ –10 mW corresponding to the prompt annihilations, followed by a 20- μ s-long tail with a peak intensity of $I = 20$ –40 μ W caused by the delayed annihilations. The hatched area represents the contribution of the $\pi^+ \rightarrow \mu^+ \rightarrow e^+$ background, and contains 50–60% of the delayed photoelectrons.

5. Gateable fine-mesh photomultiplier

According to the above simulations, a photomultiplier with a gain $g \sim 5 \times 10^4$ should detect the microwatt-scale Cherenkov light produced by the delayed annihilations as a voltage signal with an amplitude of a few hundred millivolts, terminated with a 50- Ω impedance. Unfortunately, the 5–10 mW flash of Cherenkov light caused by the prompt annihilation would normally saturate the photomultiplier and blind it during the delayed annihilation. Gateable photomultipliers [39] were therefore used, in which the electron multiplication could be turned off during the prompt annihilation. We commissioned Hamamatsu Photonics K.K. to manufacture four types of gateable photomultipliers, the specifications of which are listed in Table 2.

The diagram of the voltage divider circuit used in one of these photomultipliers (R5505GX-ASSY) is shown in Fig. 8. The dynodes are labeled as D1, D2, D3, etc., with D1 being the closest dynode to the photocathode. The tube was gated off by high-voltage transistor switches which reversed the electric potentials on the four dynodes D2, D4, D6, and D8 simultaneously, thus causing

Table 2

Specifications of the gateable photomultipliers studied here. The potential difference between the photocathode and first dynode at a photomultiplier gain $g = 5 \times 10^4$ is denoted by ΔV_{K-D1}

	R4275-02/C1392-12	R3234-01-ASSY	R5504GX-ASSY	R5505GX-ASSY
Photocathode type	Bialkali	Bialkali	Multialkali	Bialkali
Photocathode diam	46 mm	10 mm	34 mm	17.5 mm
Dynode type	Line-focus	Line-focus	Fine-mesh	Fine-mesh
Dynode stages	8	12	19	15
Switching dynodes	D2,D4	D1–D8	D1–D8	D2,D4,D6,D8
Switching ratio	1×10^3	1×10^5	5×10^5	5×10^5
ΔV_{K-D1}	320 V	280 V	110 V	140 V
Anode rise time	2.1 ns	1.4 ns	2.7 ns	1.6 ns
Anode fall time	5.2 ns	3.8 ns	6.7 ns	4.3 ns

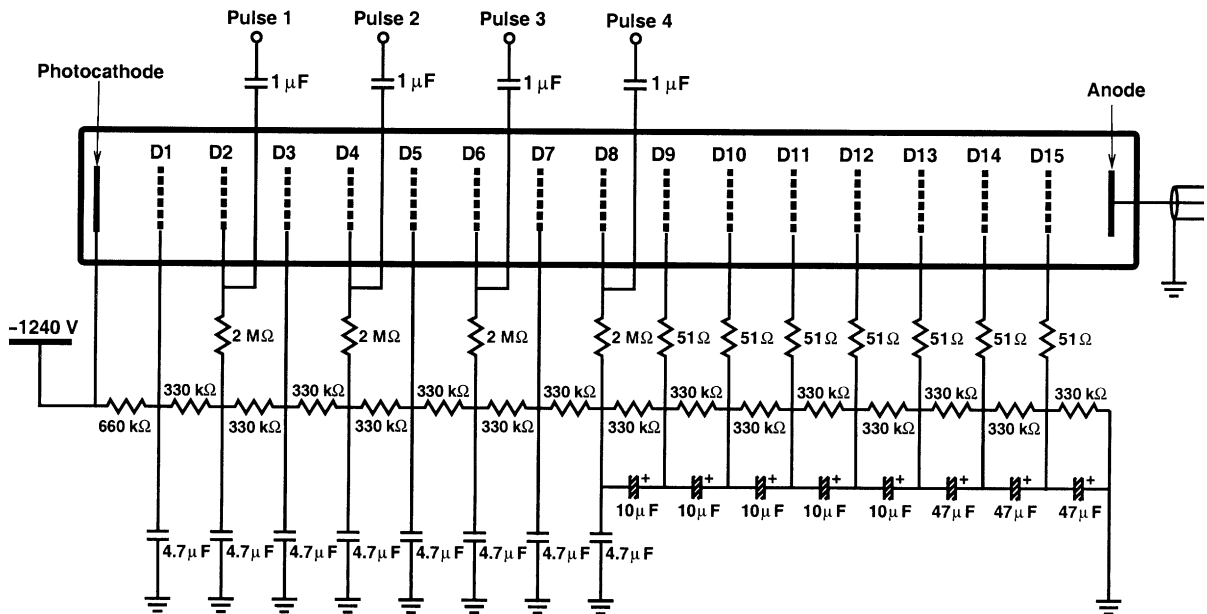


Fig. 8. Diagram of the voltage divider circuit used in the fine-mesh photomultiplier (Hamamatsu Photonics R5505GX-ASSY). The electron multiplication was gated off by reversing the potentials on dynodes D2, D4, D6, and D8 simultaneously.

the electrons traveling between some of the dynodes to be decelerated instead of being accelerated. The photomultiplier gain, which was normally adjusted to a value of $g = 5 \times 10^4$, was thus reduced by a switching ratio of $r_{sw} = 5 \times 10^5$ (Table 2). After the gate, the photomultiplier returned to its normal gain within $\Delta t \sim 150$ ns.

In order to optimize the linearity of the photomultiplier, (i) large bypass capacitors ($C = 10\text{--}47 \mu\text{F}$) were connected between the last 8 dynodes (D8–D15), (ii) the photocathode was

directly connected to a high-voltage supply with a low output impedance. The photomultiplier was thus able to produce linear signals with pulse-lengths of up to $\Delta t = 10 \mu\text{s}$ and amplitudes of up to 0.5 V, terminated with a 50- Ω impedance. For shorter pulses of $\Delta t = 100$ ns duration or less, the linearity was maintained even for signal amplitudes up to 10 V.

The timing response of the photomultipliers for short light pulses was important in our experiment, since the nanosecond-scale Auger lifetimes

of several states in $\bar{p}\text{He}^+$ were derived by measuring the decay times (Fig. 1(c)) of the laser-induced annihilation spikes [8,19]. In Fig. 9(a), the anode signal of the above photomultiplier (R5505GX-ASSY) is shown. It was detected by injecting a 100-ps-long light pulse into the photocathode, and using a voltage divider circuit without the damping resistors ($R = 51 \Omega$) shown in Fig. 8. The signal had fast rise ($\tau_r = 1.7 \text{ ns}$) and fall ($\tau_f = 3.4 \text{ ns}$) times, although ringing was observed at about 8% of the main pulse amplitude for $\Delta t \sim 10 \text{ ns}$ after it. In Fig. 9(b), the signal measured with damping resistors [40] connected to the last 7 dynodes (D9–D15) is shown. Although the resulting fall-time was longer ($\tau_f = 4.3 \text{ ns}$), the amplitude of the ringing was diminished to about 1.5% of the main pulse.

The experimental setup shown in Fig. 10 was used to measure the response of these photomultipliers when a strong light pulse was injected into them. To simulate the prompt annihilation, we

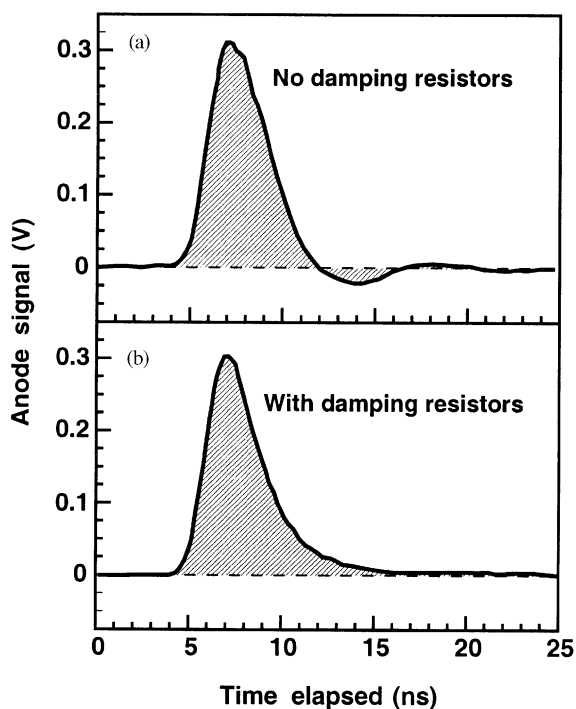


Fig. 9. Response of the fine-mesh photomultiplier (R5505GX-ASSY) to a 100-ps-long light pulse, measured without (a) and with (b) damping resistors.

constructed a light source (Fig. 10, top left) which consisted of 45 InGaA/P light emitting diodes (LED's, Toshiba TOSBRIGHT TLGE183P), each with a diameter of $d = 5 \text{ mm}$ and arranged in a semi-circular configuration with a total diameter of $d = 40 \text{ mm}$. The LED's were fitted with miniature focusing lenses which produced a uni-directional beam of light, with a full opening angle of $\theta = 10^\circ$, a wavelength of $\lambda \sim 575 \text{ nm}$, and an intensity of $\rho = 5\text{--}10 \text{ cd}$. A pulsed current of $I = 50\text{--}100 \text{ mA}$ was provided to each LED by the driving circuit shown in Fig. 10. To evenly illuminate the entire surface of the photocathode, a circular holographic diffuser (manufactured by Physical Optics Corporation) with a diffusing angle of $\theta = 30^\circ$ and transmission efficiency of 85% was positioned between the light source and photomultiplier. The absolute intensity of the light flash was calibrated using a silicon photodiode (Hamamatsu Photonics S1337-1010BQ). Measurements were made with the following procedure: (i) the photomultiplier under test was gated off, (ii) the light source was flashed on at $t = 0$, thus irradiating the photocathode with a 100-ns-long pulse with a peak intensity of $I = 5 \text{ mW}$, (iii) the photomultiplier was switched back on at $t = 300 \text{ ns}$, and the anode waveform recorded using a digital oscilloscope.

In Fig. 11(a), the waveform of a high-speed gateable photomultiplier (R4275-02/C1392-12MOD) with a 46-mm-diam bialkali photocathode and 8 line-focus dynodes [40] is shown. The potentials on dynodes D2 and D4 were reversed during the arrival of the 5-mW light pulse, thus achieving a switching ratio of $r_{\text{sw}} = 10^3$. Since the photomultiplier's effective gain was reduced to a value of $g/r_{\text{sw}} \sim 50$, a highly diminished signal with an amplitude of $\sim 500 \text{ mV}$ was observed at $t = 0$. The photomultiplier was reactivated by returning the two dynodes to their normal values. Ideally, no signal should afterwards emerge from the anode, but as shown in Fig. 11(a), four spurious afterpulses with amplitudes of 100–400 mV were seen at $t_1 = 0.6 \mu\text{s}$, $t_2 = 1.1 \mu\text{s}$, $t_3 = 1.9 \mu\text{s}$, and $t_4 = 2.8 \mu\text{s}$.

In Fig. 11(b), the afterpulses of a R3234-01-ASSY photomultiplier with a 10-mm-diam, bialkali photocathode and 12 line-focus dynodes is

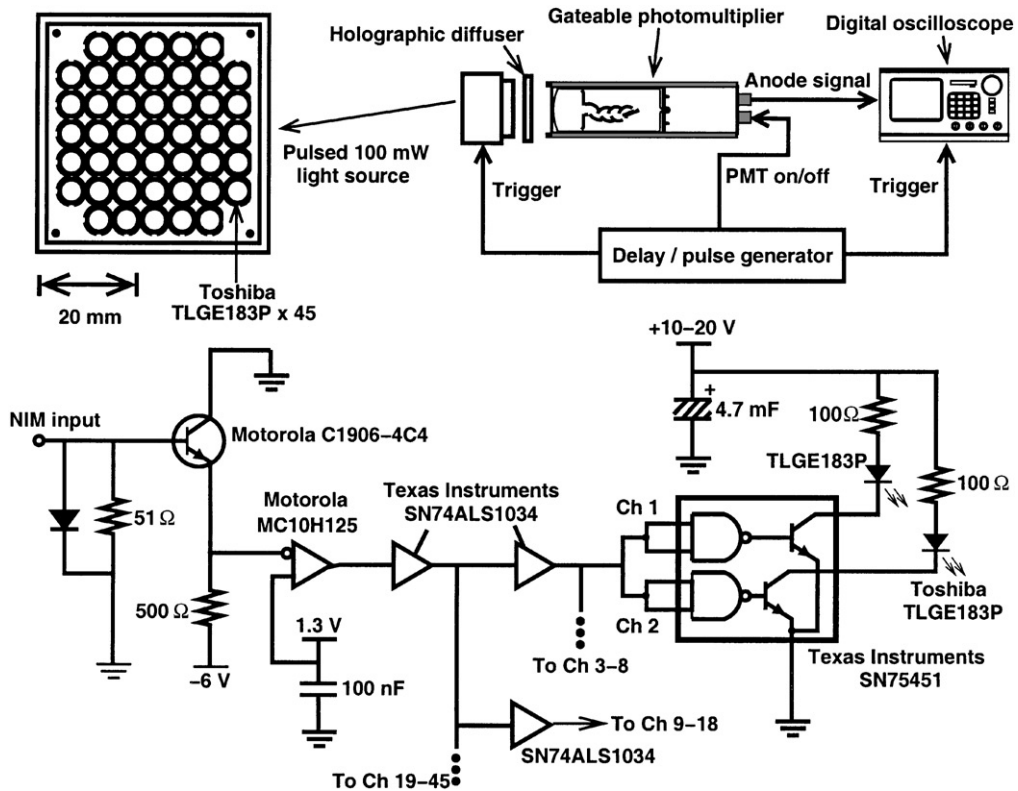


Fig. 10. Schematic drawing of the LED light source to simulate the prompt annihilation (top left), and the circuit diagram of the high-current pulser used to drive it (bottom). Experimental setup to measure the afterpulse characteristics of photomultipliers (top right).

shown. This detector was recommended by the manufacturer for high-speed single-photon counting applications, and designed to have reduced afterpulsing. The potentials on the first eight dynodes (D1–D8) were reversed during gating. It was hoped that the dynodes would absorb the ion pairs produced by the light flash, and prevent the afterpulsing. The switching ratio of the detector was so high ($r_{sw} = 1 \times 10^5$) that the signal from the 5-mW flash was almost completely suppressed by the gating (Fig. 11(b)). Two afterpulses at $t_1 = 0.6 \mu\text{s}$ and $t_2 = 0.95 \mu\text{s}$ were observed, but unlike the R4275-02/C1392-12MOD, no strong afterpulses were detected after $t \sim 1 \mu\text{s}$.

In Fig. 11(c), the afterpulse response of a fine-mesh photomultiplier [41,42] (R5504GX-ASSY) with a 34-mm-diam multialkali photocathode is shown. The photomultiplier had 19 dynodes, each consisting of a fine mesh with a geometrical transmission of about 50% and a pitch of

1500 meshes/in. The spacing between neighboring dynodes was less than $d = 1 \text{ mm}$, while the distance between the photocathode and first dynode was less than $d = 3 \text{ mm}$. The potentials on the eight dynodes D1–D8 were reversed during the gating, thus achieving a switching ratio of $r_{sw} = 5 \times 10^5$. The afterpulse had a length of $\Delta t \sim 0.5 \mu\text{s}$ and a small amplitude, the major part of which disappeared after $t \sim 0.7 \mu\text{s}$. In Fig. 11(d), the response of a fine-mesh photomultiplier (R5505GX-ASSY) with a 17.5-mm-diam bialkali photocathode and 15 dynodes is shown. As described above, the potentials on the four dynodes D2, D4, D6, and D8 were reversed during the gate. The amplitude of the afterpulse was similar or slightly larger than that of the R5504GX-ASSY.

In Fig. 12(a), the ratios between the charge Q_{after} in the afterpulse and the total charge Q_{total} in the anode signal are plotted. The photomultiplier gain

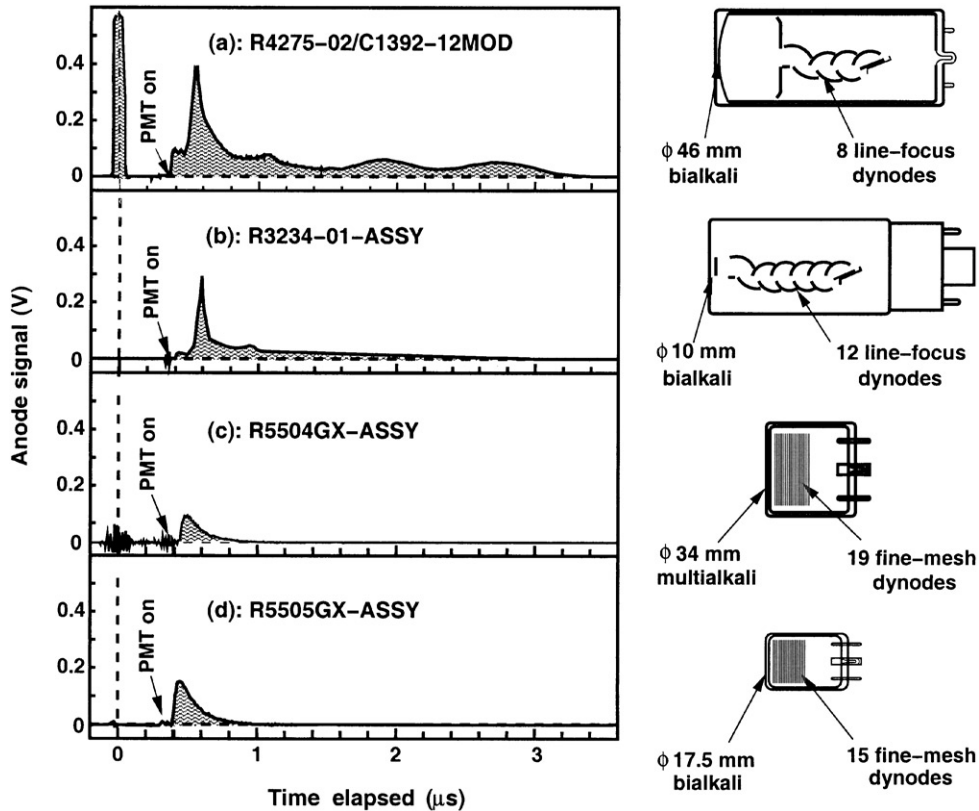


Fig. 11. Afterpulse characteristics of four types of gateable photomultipliers (a)–(d). They were gated off during the strong light pulse at $t = 0$, and reactivated at $t = 300$ ns. Schematic diagrams of the four photomultipliers (right).

was kept constant at a value of $g = 5 \times 10^4$, while the intensity of the light pulse was varied between values corresponding to a total anode charge of $Q_{\text{total}} = 200$ and 1000 pC. Measurements were made using three identical fine-mesh photomultipliers (R5505GX-ASSY), and the three sets of results were plotted by filled circles, triangles, and squares. The afterpulse intensities varied by a factor of ~ 2 among the photomultipliers, possibly due to variations in manufacturing or handling. The ratio $Q_{\text{after}}/Q_{\text{total}}$ remained constant at about $(6\text{--}12) \times 10^{-4}$, with little or no dependence on the light intensity.

We next measured the afterpulse amplitudes at various values of the photomultiplier gain and a fixed intensity of the light pulse. As shown in Fig. 12(b), the ratio $Q_{\text{after}}/Q_{\text{total}}$ increased dramatically from $(6\text{--}13) \times 10^{-4}$ to $(1.5\text{--}3) \times 10^{-2}$ as

the gain was changed from $g = 1 \times 10^4$ (corresponding to a potential difference of $\Delta V_{\text{K-D1}} = 110$ V between the photocathode and first dynode) to 5×10^6 (corresponding to a $\Delta V_{\text{K-D1}}$ value of 280 V).

Although the afterpulsing in line-focus photomultipliers has been studied for the past 40 years, the mechanisms that cause them are not fully understood [40]. In Ref. [43], it is argued that afterpulsing is mainly caused by photoelectrons ionizing the residual gases in the volume between the photocathode and first dynode. The positive ions drift towards the photocathode and strike its surface, releasing secondary electrons. These are amplified by the electron multiplier and emerge from the anode as an afterpulse. The authors point out that the electric fields in a line-focus photomultiplier are such that the transit time for an ion

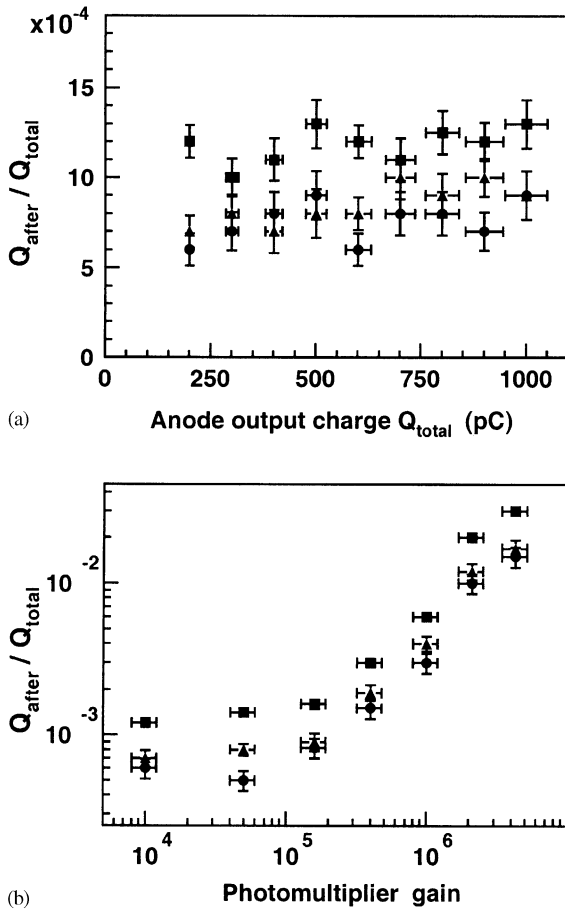


Fig. 12. Ratio between the charge Q_{after} in the afterpulse and the total charge Q_{total} in the anode signal (a), measured at a fixed photomultiplier gain $g = 5 \times 10^4$ and varying the intensity of the light pulse. The ratio $Q_{\text{after}}/Q_{\text{total}}$ measured at various values of the gain, and a fixed light intensity (b).

of a given mass and charge to reach the photocathode is nearly independent of its point of origin. Since the ions arrive at the photocathode nearly simultaneously, a sharp afterpulse is produced, the delay time t being determined by its mass and charge. In experiments using a line-focus photomultiplier, it was found that 3–4 secondary electrons were emitted from the photocathode per incident H_2^+ ion which caused a large afterpulse to appear at $t = 0.3 \mu\text{s}$. In contrast, a N_2^+ ion produced only a single electron which led to a relatively weak afterpulse at $t = 1.2 \mu\text{s}$. Afterpulses caused by Ar^+ and Xe^+ ions were detected at $t =$

1.3 and $2.5 \mu\text{s}$, respectively. In Ref. [44], it is reported that afterpulses can also be produced by single ions such as H^+ , He^+ , and O^+ . The author argues that these ions can originate inside the electron multiplier, as well as from the volume between the photocathode and first dynode. Recent theoretical [45] and experimental [46,47] studies support the above references. We therefore assumed that the strong afterpulse which appears at $t = 0.6 \mu\text{s}$ in Fig. 11(a) is due to H_2^+ ions striking the photocathode. In Ref. [48], the increase of the afterpulse over long periods of time caused by diffusion of helium gas through the glass window of the photomultiplier was studied. Although the photomultipliers used in the present experiments were operated for several weeks near a helium target, we detected no significant increase in the afterpulse amplitudes. It has also been reported that gating the photomultiplier during a strong flash of light can significantly reduce the afterpulse [49,50].

In the line-focus photomultipliers studied here, sharp afterpulses with large amplitudes were observed, whereas in fine-mesh photomultipliers the afterpulses were much longer with smaller amplitudes. The reasons for these differences are not understood. A possible explanation is that in fine-mesh photomultipliers, the positive ions produced by gas ionization along the trajectory of the photoelectrons arrive at the photocathode with a broad timing distribution due to the parallel electric fields between the electrodes, while in line-focus photomultipliers the ions arrive almost simultaneously as described above. Furthermore, at the photomultiplier gain of $g = 5 \times 10^4$ used in these experiments, the potential difference between the photocathode and first dynode D1 in the line-focus photomultipliers were much larger ($\Delta V_{\text{K-D1}} \sim 300 \text{ V}$, see Table 2) compared to the corresponding values in the fine-mesh photomultipliers ($\Delta V_{\text{K-D1}} = 110\text{--}140 \text{ V}$). Since the yield γ_{sec} of secondary electrons emitted from the photocathode is strongly dependent on the energy of the ions striking its surface [51], we expect that more of them are produced per incident ion in line-focus photomultipliers compared to fine-mesh ones. This assumption is partially supported by the experimental results of Fig. 12(b), which show that as the

ΔV_{K-D1} value was increased from 110 to 280 V in a fine-mesh photomultiplier (R5505GX-ASSY) by increasing the gain from $g = 1 \times 10^4$ to 5×10^6 , the relative intensity of the afterpulses increased drastically from $Q_{\text{after}}/Q_{\text{total}} = (6-13) \times 10^{-4}$ to $(1.5-3) \times 10^{-2}$.

6. Experimental results with $\bar{p}\text{He}^+$ atoms

The waveform shown in Fig. 13(a) was detected by the ungated Cherenkov detector when a pulse containing 5×10^8 antiprotons was stopped in the helium target. A fine-mesh photomultiplier (R5504GX-ASSY) was used at a gain of $g = 1 \times 10^3$. The prompt annihilation is clearly seen as a 250-ns-long pulse, but the signal corresponding to the delayed annihilation of $\bar{p}\text{He}^+$ is so weak that it is barely visible. In Fig. 13(b), the spectrum measured at the same beam intensity but with a higher gain of $g = 5 \times 10^4$ is shown. The initial light flash saturated the photomultiplier, and an abnormal drop of the anode signal below ground potential was seen which continued until $t \sim 50$ μs . In Fig. 14(c) the result of gating the photomultiplier during the prompt annihilation is shown. The delayed annihilation is now clearly detected as a 300–700-mV signal. All subsequent measurements were made under these conditions.

The delayed annihilation time spectrum shown in Fig. 14(a) was measured at a beam intensity of 5×10^8 antiprotons per pulse and using the line-focus photomultiplier (R4275-02/C1392-12MOD). The laser annihilation spike corresponding to the $\bar{p}\text{He}^+$ transition $(n, \ell) = (37, 35) \rightarrow (38, 34)$ at a wavelength of $\lambda = 726.1$ nm was induced at $t = 1$ μs in the spectrum. The strong afterpulse appearing at $t \sim 0.5$ μs made the detection of weak transitions at early times ($t < 0.7$ μs) difficult or impossible, since the laser-induced annihilation spikes could not be easily distinguished from the afterpulses. In contrast, the spectrum measured using the fine-mesh photomultiplier (R5504GX-ASSY) contained no significant afterpulses (Fig. 14(b)). Clear annihilation spikes could hence be induced at much earlier ($t \sim 0.3$ μs) times.

In Fig. 14(c), the electric charge in the anode signal integrated over the time interval between

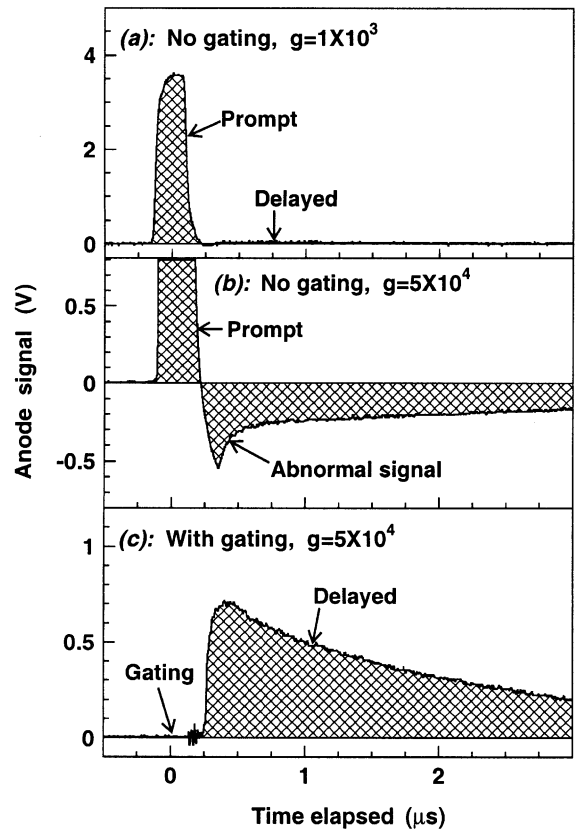


Fig. 13. The prompt annihilation produced by 5×10^8 antiprotons stopping in the helium target (a), measured at a photomultiplier gain $g = 1 \times 10^3$. The spectrum measured at the same beam intensity and with $g = 5 \times 10^4$ (b). The delayed annihilation time spectrum (c) measured when the photomultiplier was gated off during the prompt annihilation and reactivated at $t = 250$ ns.

$t = 0$ and 20 μs is shown, measured at various beam intensities between 4×10^7 and 4×10^8 antiprotons per pulse. The fine-mesh photomultiplier (R5504GX-ASSY) showed a linear response, whereas the line-focus photomultiplier (R4275-02/C1392-12MOD) had a highly non-linear response. The observed differences are presumably due to the fact that in fine-mesh photomultipliers, large numbers of electrons can be accelerated in the uniform electric fields between the mesh dynodes without reaching a high space-charge density, whereas in line-focus photomultipliers the electrons are strongly focused, causing space-charge effects in the later stages of the electron multiplier.

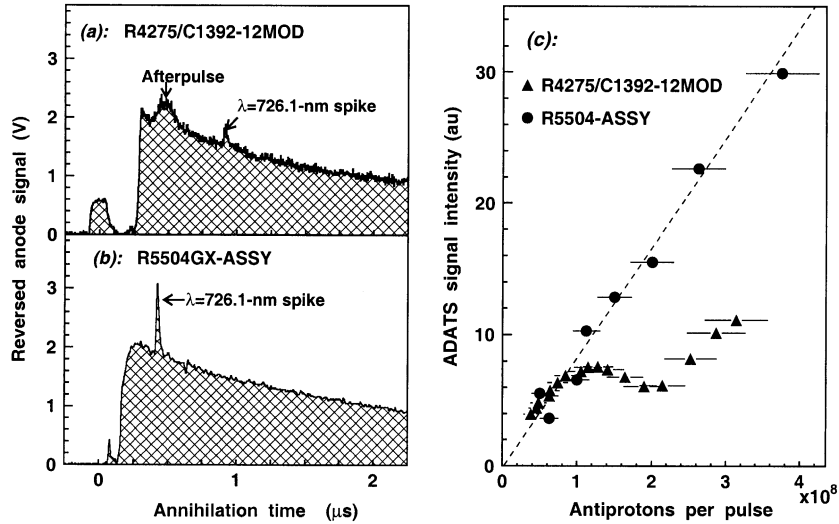


Fig. 14. Delayed annihilation time spectra measured using a line-focus (R4275-02/C1392-12MOD) photomultiplier (a), with the transition $(n, \ell) = (37, 35) \rightarrow (38, 34)$ at a wavelength of $\lambda = 726.1$ nm induced at $t = 1$ μ s. The spectrum measured using a fine-mesh photomultiplier (R5504GX-ASSY) (b), with the spike induced at $t = 0.4$ s. Total charge in the anode signals (c) of the two photomultipliers measured at various intensities of the antiproton beam.

Using this Cherenkov detector with fine-mesh photomultiplier, it became possible to induce and detect extremely weak transitions at early times in the delayed annihilation time spectrum, which had never been observed before [13]. In Fig. 15(a)–(e), the spectra measured using a helium target with a 100-ppm admixture of molecular hydrogen, at pressure $P = 5$ bar and temperature $T = 30$ K is shown [13]. The laser was fired at $t = 0.3$ μ s in each spectrum, the wavelength λ being varied as indicated. The small peak which appears as the laser wavelength approaches $\lambda = 597.297$ nm corresponds to the transition $(n, \ell) = (38, 35) \rightarrow (39, 36)$. Normally, this transition cannot be observed because both parent and daughter states are metastable with 1- μ s lifetimes, while according to the discussion of Section 1, the laser pulse can produce an annihilation spike only if the lifetimes of the two states differ substantially. It was found, however, that collisions between $\bar{p}\text{He}^+$ atoms and hydrogen molecules selectively shorten the lifetimes of states having high n -values (i.e. $(39, 36)$ in this case) while leaving the lifetimes of the lower- n states (i.e. $(38, 35)$) relatively unchanged. By adding small admixtures of hydrogen in the target,

we were therefore able to detect four transitions: $(38, 35) \rightarrow (39, 36)$ at a wavelength of $\lambda = (597.298 \pm 0.002)$ nm (the resonance profile of which is shown in Fig. 15(f)), $(38, 36) \rightarrow (39, 37)$ at (597.397 ± 0.002) nm (Fig. 15(g)), $(38, 37) \rightarrow (39, 38)$ at (597.607 ± 0.002) nm (Fig. 15(h)), and $(37, 36) \rightarrow (38, 37)$ at (597.930 ± 0.002) nm (Fig. 15(i)).

The stability and reproducibility of the experiment was studied by measuring the transition $(n, \ell) = (37, 34) \rightarrow (36, 33)$ at a wavelength of $\lambda = 470.7$ nm. In Fig. 16(a), the intensities of ten antiproton pulses stopped consecutively in the helium target are shown, the number of antiprotons in each pulse decreasing from 5×10^8 to 5×10^7 . In Fig. 16(b), the energies of the laser pulses irradiating the $\bar{p}\text{He}^+$ atoms are shown. The energy fluctuated by about $\pm 20\%$, due to instabilities in the excimer-pumped dye lasers used in these experiments [5,6]. In Fig. 16(c), the corresponding intensities of the laser-induced annihilation spikes are shown, normalized to the total number of stopped antiprotons. This fluctuated by $\pm 22\%$, probably due to instabilities in the timing profiles and wavelengths of the laser pulses.

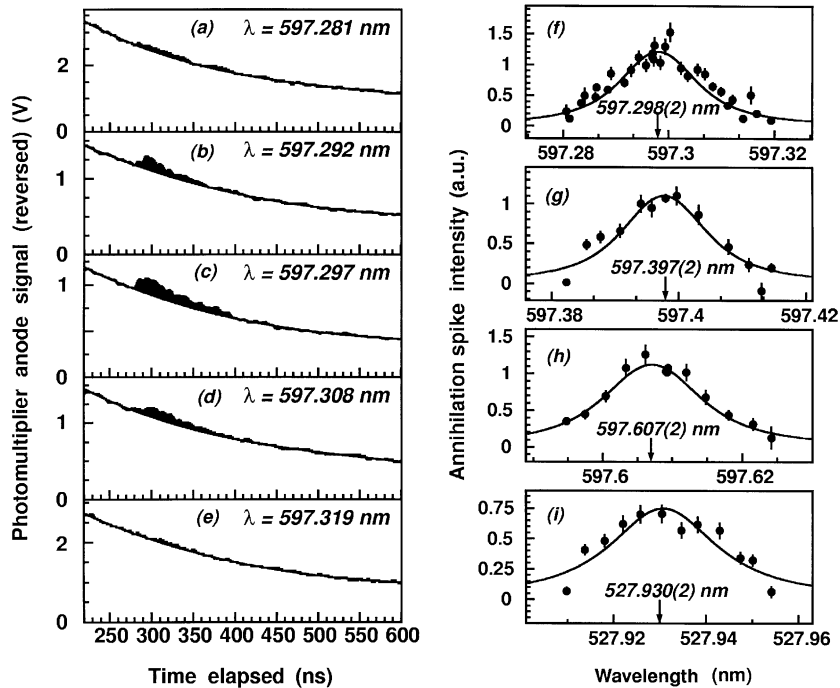


Fig. 15. Delayed annihilation time spectra (a)–(e) measured using a helium target at a pressure of $P = 5$ bar and temperature of $T = 30$ K, with a 100-ppm admixture of molecular hydrogen. Laser pulses with the indicated wavelengths λ are irradiated at $t = 0.3$ μ s. The spike intensities as a function of laser wavelength, for the transitions (38, 35) \rightarrow (39, 36) (f), (38, 36) \rightarrow (39, 37) (g), (38, 37) \rightarrow (39, 38) (h), and (37, 36) \rightarrow (38, 37) (i). All figures taken from Ref. [13].

7. Comparisons with experiments using continuous antiproton beams

We compared the experimental data measured using pulsed antiproton beams in the present work, with those measured using continuous antiproton beams in past experiments. In the latter type of experiment [5,6,8], antiprotons were continuously injected into the helium target at rate of 10^4 \bar{p} /s, so that on average only a single metastable $\bar{p}\text{He}^+$ atom existed inside the target at a time (Fig. 17). The arrival of antiprotons was detected by a 0.5 mm-thick plastic scintillation counter, which was placed in the beam upstream of the target. Each annihilation was identified with $99.7 \pm 0.1\%$ efficiency by seven shower counters surrounding the target, which detected at least two of the five π -mesons typically produced in an annihilation event. The time of annihilation was thus measured relative to the time of passage of the

antiprotons through the beam counter, one particle at a time. In this way, a background-free spectrum containing $\sim 10^6$ delayed annihilations of metastable atoms was obtained. The laser pulses reached the atom at a time $t = 1.8$ μ s or later, as this was the minimum delay achievable by the method of identifying the randomly occurring metastable events, and then triggering the lasers.

The delayed annihilation time spectrum shown in Fig. 18(a) was measured by stopping a pulse of 2×10^8 antiprotons in the helium target at pressure $P = 0.6$ bar and temperature $T = 5.8$ K. The transition $(n, \ell) = (39, 35) \rightarrow (38, 34)$ at a wavelength of $\lambda = 597.26$ nm is induced at $t = 1.6$ μ s. In Fig. 18(b), the spectra measured at the same experimental conditions, but using a continuous antiproton beam is shown. The number of events in the laser-induced spike should be the same in both spectra when normalized to the total number of stopped antiprotons. By comparing the

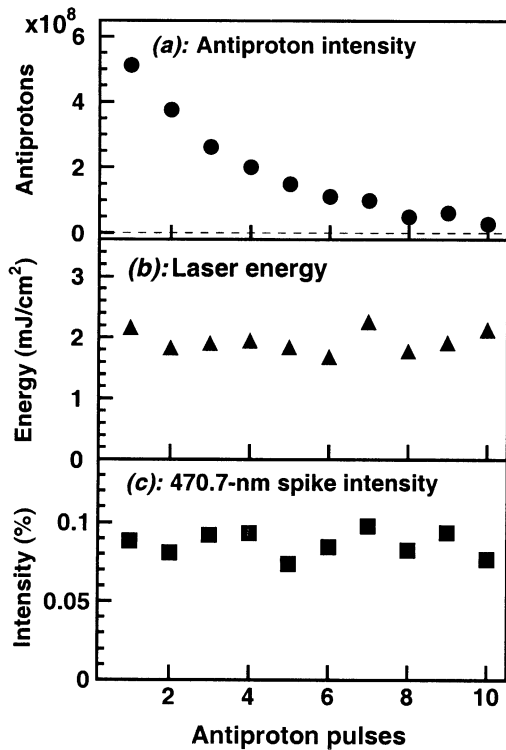


Fig. 16. The intensities of 10 consecutive antiproton (a) and corresponding laser (b) pulses arriving at the target. The normalized intensities of the resulting laser-induced annihilation spikes (c) of the transition $(n, \ell) = (37, 34) \rightarrow (36, 33)$ at a wavelength of $\lambda = 470.7$ nm.

intensities of the two spikes, therefore, we were able to estimate that the $\pi^+ \rightarrow \mu^+ \rightarrow e^+$ background (which appears in the former spectrum, but not the latter) constitutes 50–60% of the Cherenkov light as represented by the hatched area. This estimation agrees with the results of the Monte Carlo simulation shown in Fig. 7(c).

8. Experiments at the antiproton decelerator

The LEAR facility was closed in 1996, and replaced by the Antiproton Decelerator (AD) [16] which began operation in 1999. Laser spectroscopy experiments of $\bar{p}\text{He}^+$ atoms were there continued by the Antiproton Spectroscopy And Collisions Using Slow Antiprotons (ASACUSA) collaboration [15,17–20], as shown in the experi-

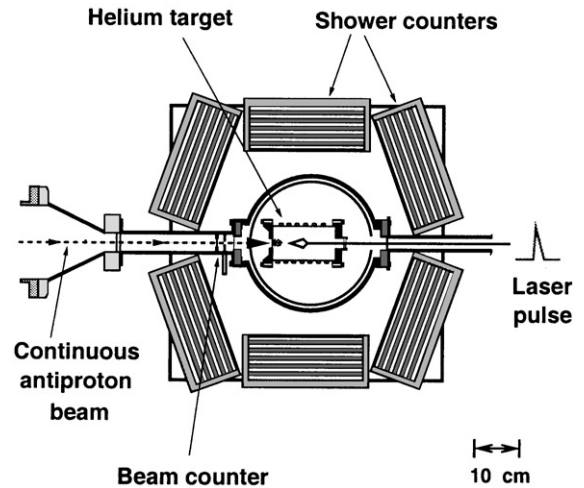


Fig. 17. Layout of the laser spectroscopy experiment of $\bar{p}\text{He}^+$ using a continuous antiproton beam. Individual antiprotons are stopped in the target at a rate of 10^4 \bar{p} /s, and the lifetime of each atom is measured as the time elapsed from antiproton incidence (supplied by the beam counter) to annihilation (supplied by the seven shower counters surrounding the target).

mental layout of Fig. 19. The AD produced a pulsed beam containing 3×10^7 antiprotons at an energy $T = 5.3$ MeV and repetition rate $f = 0.01$ Hz. Due to the lower energies, the antiprotons could be stopped in a much smaller volume of helium gas compared to the LEAR experiments (Fig. 2) which were made using 21-MeV antiprotons. Two small Cherenkov detectors made of UV-transparent acrylic (Mitsubishi Rayon, Acrylite-000) measuring $300 \text{ mm} \times 100 \text{ mm} \times 20 \text{ mm}$ covered a solid angle of 2π steradians seen from the target. The Cherenkov detectors were read out by fine-mesh photomultipliers (R5505GX-ASSY) with 17.5-mm-diam bialkali photocathodes (Table 2). Due to the smaller construction of the Cherenkov radiators and photomultipliers, the anode signals had faster rise ($t_r = 1.5$ ns) and fall ($t_f = 2.3$ ns) times, and larger photoelectron yields ($\langle \gamma_{\bar{p}} \rangle = 10\text{--}15$) than those used previously at LEAR.

In Fig. 20(a), a delayed annihilation time spectrum is shown with the annihilation spike of the transition $(n, \ell) = (35, 33) \rightarrow (34, 32)$ at a wavelength of $\lambda = 372.6$ nm induced at $t = 5$ μs . The fast timing response of the detector allowed us to

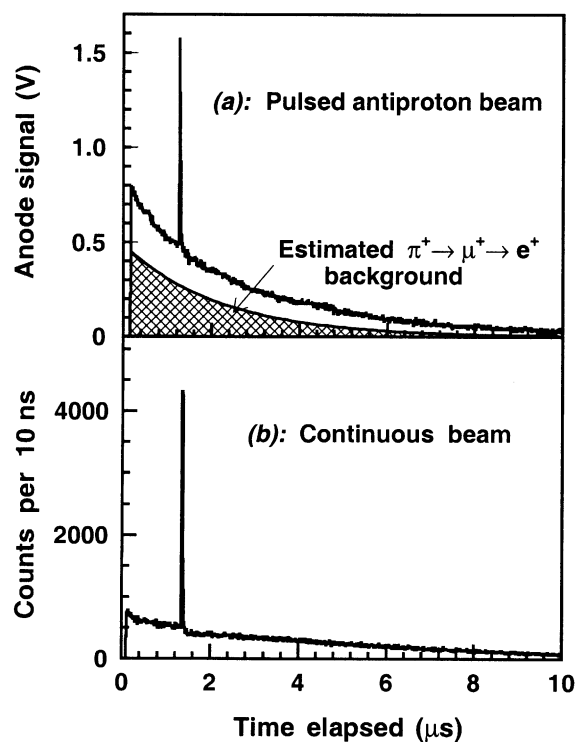


Fig. 18. Delayed annihilation time spectra measured by stopping a pulse of 2×10^8 antiprotons in a helium target (a). The transition $(n, \ell) = (39, 35) \rightarrow (38, 34)$ at a wavelength of $\lambda = 597.26$ nm is induced at $t = 1.6$ μs . The hatched area represents the contribution from $\pi^+ \rightarrow \mu^+ \rightarrow e^+$ background. The background-free, delayed annihilation time spectrum measured using the continuous antiproton beam (b).

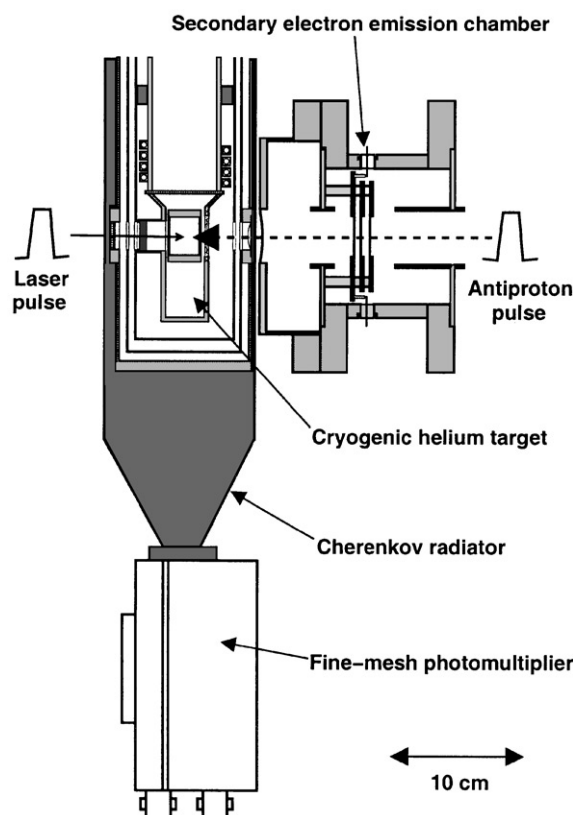


Fig. 19. Layout of laser spectroscopy experiment of $\bar{p}\text{He}^+$ carried out at AD.

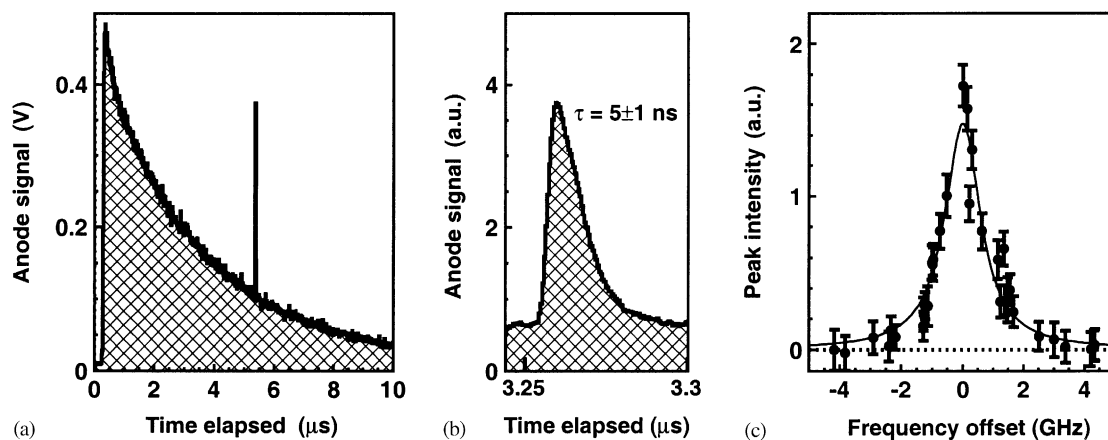


Fig. 20. Typical delayed annihilation time spectrum measured at AD (a). Expanded view of the laser-induced annihilation spike corresponding to the transition $(n, \ell) = (35, 33) \rightarrow (34, 32)$ at a wavelength of $\lambda = 372.6$ nm (b). Resonance scan of the 372.6-nm transition (c).

accurately measure the decay rates of the annihilation spikes (Fig. 20(b)), from which we deduced the Auger lifetimes of the atomic states ($\tau_{(34,32)} = 5 \pm 1$ ns in this case) [17,19]. In Fig. 20(c), the spike intensity is plotted as a function of the laser wavelength. From resonance scans such as those shown here, we were able to derive the atomic transition frequencies of $\bar{p}\text{He}^+$ to fractional precisions between 1.3×10^{-7} and 1.6×10^{-6} [17].

Acknowledgements

We would like to thank the members of the ASACUSA and PS205 collaborations. We are deeply indebted to Hamamatsu Photonics K.K. for their untiring efforts in designing and manufacturing the gated fine-mesh photomultipliers used in these experiments. We thank the CERN PS division and the KEK-Tanashi ES crew for their help. The developmental work on the Cherenkov detectors was supported by two grants from Monbukagakusho of Japan: the Grant-in-Aid for Specially Promoted Research and for International Scientific Research, and the Grant-in-Aid for Creative Basic Research (10NP0101).

References

- [1] M. Iwasaki, S.N. Nakamura, K. Shigaki, Y. Shimizu, H. Tamura, T. Ishikawa, R.S. Hayano, E. Takada, E. Widmann, H. Oota, M. Aoki, P. Kitching, T. Yamazaki, *Phys. Rev. Lett.* **67** (1991) 1246.
- [2] T. Yamazaki, N. Morita, R. Hayano, E. Widmann, J. Eades, *Phys. Rep.* **366** (2002) 183.
- [3] V.I. Korobov, D.D. Bakalov, *Phys. Rev. Lett.* **79** (1997) 3379.
- [4] N. Morita, K. Ohtsuki, T. Yamazaki, *Nucl. Instr. and Meth. A* **330** (1993) 439.
- [5] N. Morita, et al., *Phys. Rev. Lett.* **72** (1994) 1180.
- [6] H.A. Torii, et al., *Nucl. Instr. and Meth. A* **396** (1997) 257.
- [7] H.A. Torii, et al., *Phys. Rev. A* **59** (1999) 223.
- [8] M. Hori, et al., *Phys. Rev. A* **57** (1998) 1698; M. Hori, et al., *Phys. Rev. A* **58** (1998) 1612.
- [9] R.S. Hayano, et al., *Phys. Rev. Lett.* **73** (1994) 1485; R.S. Hayano, et al., *Phys. Rev. Lett.* **73** (1994) 3181.
- [10] A. Nistroj, et al., *Nucl. Instr. and Meth. A* **373** (1996) 411.
- [11] S. Baird, J. Bossler, M. Chanel, P. Lefèvre, R. Ley, D. Manglunki, S. Maury, D. Möhl, G. Tranquille, *Hyperfine Interactions* **76** (1993) 61.
- [12] M. Chanel, LEAR Performance, Proceedings of the LEAR Symposium, CERN, Geneva, 1998, CERN/PS 99-040 (CA), CERN, Geneva, 1999.
- [13] B. Ketzer, et al., *Phys. Rev. Lett.* **78** (1997) 1671.
- [14] T. Yamazaki, et al., *Phys. Rev. A* **55** (1997) R3295.
- [15] M. Hori, *Nucl. Phys. A* **692** (2001) 119.
- [16] T. Erikson, S. Maury, D. Möhl, *Nucl. Phys. A* **692** (2001) 187.
- [17] M. Hori, J. Eades, R.S. Hayano, T. Ishikawa, J. Sakaguchi, E. Widmann, H. Yamaguchi, H.A. Torii, B. Juhász, D. Horváth, T. Yamazaki, *Phys. Rev. Lett.* **87** (2001) 093401.
- [18] B. Juhász, J. Eades, R.S. Hayano, M. Hori, D. Horváth, T. Ishikawa, J. Sakaguchi, H.A. Torii, E. Widmann, H. Yamaguchi, T. Yamazaki, *Eur. Phys. J. D* **18** (2002) 261.
- [19] H. Yamaguchi, T. Ishikawa, J. Sakaguchi, E. Widmann, J. Eades, R.S. Hayano, M. Hori, H.A. Torii, B. Juhász, D. Horváth, T. Yamazaki, *Phys. Rev. A* **66** (2002) 022504.
- [20] M. Hori, J. Eades, R.S. Hayano, T. Ishikawa, J. Sakaguchi, T. Tasaki, E. Widmann, H. Yamaguchi, H.A. Torii, B. Juhász, D. Horváth, T. Yamazaki, *Phys. Rev. Lett.* **89** (2002) 093401.
- [21] M. Hori, *Nucl. Instr. and Meth. A*, to be submitted.
- [22] G. Keil, *Nucl. Instr. and Meth.* **87** (1970) 111.
- [23] P. Montagna, et al., *Nucl. Phys. A* **700** (2002) 159.
- [24] A. Adamo, et al., *Nucl. Phys. A* **569** (1994) 761.
- [25] C. Amsler, et al., *Z. Phys. C* **58** (1993) 175.
- [26] C. Ghesquière, CERN Yellow Report 74-18 p. 436, CERN, Geneva, 1974.
- [27] S. Ahmad, et al., *Phys. Lett. B* **152** (1985) 135.
- [28] J. Sedláč, V. Šimák, *Sov. J. Part. Nucl.* **19** (1988) 191.
- [29] A. Abele, et al., *Phys. Lett. B* **411** (1997) 354.
- [30] N.S. Cesari, et al., *Nucl. Phys. A* **655** (1999) 82.
- [31] A. Abele, et al., *Phys. Lett. B* **468** (1999) 178.
- [32] A. Bettini, M. Cresti, S. Limentani, L. Peruzzo, R. Santangelo, S. Sartori, L. Bertanza, A. Bigi, R. Carrara, R. Casali, P. Lariccia, *Nuovo Cimento* **47** (1967) 642.
- [33] D. Bridges, I. Daftari, T.E. Kalogeropoulos, R. Debbe, W. Fickinger, D.K. Robinson, *Phys. Rev. Lett.* **56** (1986) 215.
- [34] F. Balestra, et al., *Nucl. Phys. A* **465** (1987) 714.
- [35] Particle Data Group, K. Hagiwara, et al., *Phys. Rev. D* **66** (2002) 010001.
- [36] G. Bendiscioli, D. Kharzeev, *Riv. Nuovo Cimento* **17** (1994) 1.
- [37] G. Bendiscioli, et al., *Nucl. Phys. A* **518** (1990) 683.
- [38] GEOMETRY AND TRACKING GEANT version 4.0, CERN, Geneva, 1999.
- [39] E. Böhm, U.J. Roose, R. Staubert, J. Trümper, *Nucl. Instr. and Meth.* **40** (1966) 67.
- [40] B.H. Candy, *Rev. Sci. Instrum.* **56** (1985) 183.
- [41] R. Enomoto, T. Sumiyoshi, K. Hayashi, I. Adachi, S. Suzuki, H. Suzuki, *Nucl. Instr. and Meth. A* **332** (1993) 129.
- [42] T. Iijima, et al., *Nucl. Instr. and Meth. A* **387** (1997) 64.
- [43] G.A. Morton, H.M. Smith, R. Wasserman, *IEEE Trans. Nucl. Sci. NS-14* (1) (1967) 443.

- [44] P.B. Coates, *J. Phys. D* 6 (1973) 1159.
- [45] S. Ohsuka, Y. Ogata, Y. Tamura, *Nucl. Instr. and Meth. A* 384 (1997) 477.
- [46] V.A. Morozov, N.V. Morozova, Effect of interelectrode potentials in the photomultiplier on formation of afterpulses, JINR-P13-2001-135, JINR, Dubna, 2001.
- [47] R. Mirzoyan, E. Lorenz, D. Petry, C. Prosch, *Nucl. Instr. and Meth. A* 387 (1997) 74.
- [48] J.R. Incandela, S.P. Ahlen, J. Beatty, A. Ciocio, M. Felcini, D. Ficenece, E. Hazen, D. Levin, A. Marin, J.L. Stone, L.R. Sulak, W. Worstell, *Nucl. Instr. and Meth. A* 269 (1988) 237.
- [49] R. Staubert, E. Böhm, K. Hein, K. Sauerland, J. Trümper, *Nucl. Instr. and Meth.* 84 (1970) 297.
- [50] S.J. Hall, J. McKeown, *Nucl. Instr. and Meth.* 112 (1973) 545.
- [51] D. Hasselkamp, H. Rothard, K.-O. Groeneveld, J. Kemmler, P. Varga, H. Winter, *Particle Induced Electron Emission II*, Springer, Berlin, Heidelberg, 1992.